



The latitudinal temperature gradient and its climate dependence as inferred from foraminiferal $\delta^{18}\text{O}$ over the past 95 million years

Daniel E. Gaskell^{a,1} , Matthew Huber^b , Charlotte L. O'Brien^c , Gordon N. Inglis^d , R. Paul Acosta^e , Christopher J. Poulsen^e , and Pincelli M. Hull^a 

Edited by James Zachos, University of California, Santa Cruz, CA; received June 18, 2021; accepted January 24, 2022

The latitudinal temperature gradient is a fundamental state parameter of the climate system tied to the dynamics of heat transport and radiative transfer. Thus, it is a primary target for temperature proxy reconstructions and global climate models. However, reconstructing the latitudinal temperature gradient in past climates remains challenging due to the scarcity of appropriate proxy records and large proxy–model disagreements. Here, we develop methods leveraging an extensive compilation of planktonic foraminifera $\delta^{18}\text{O}$ to reconstruct a continuous record of the latitudinal sea-surface temperature (SST) gradient over the last 95 million years (My). We find that latitudinal SST gradients ranged from 26.5 to 15.3 °C over a mean global SST range of 15.3 to 32.5 °C, with the highest gradients during the coldest intervals of time. From this relationship, we calculate a polar amplification factor (PAF; the ratio of change in $>60^\circ$ S SST to change in global mean SST) of 1.44 ± 0.15 . Our results are closer to model predictions than previous proxy-based estimates, primarily because $\delta^{18}\text{O}$ -based high-latitude SST estimates more closely track benthic temperatures, yielding higher gradients. The consistent covariance of $\delta^{18}\text{O}$ values in low- and high-latitude planktonic foraminifera and in benthic foraminifera, across numerous climate states, suggests a fundamental constraint on multiple aspects of the climate system, linking deep-sea temperatures, the latitudinal SST gradient, and global mean SSTs across large changes in atmospheric CO_2 , continental configuration, oceanic gateways, and the extent of continental ice sheets. This implies an important underlying, internally driven predictability of the climate system in vastly different background states.

latitudinal temperature gradients | meridional temperature gradients | sea-surface temperatures | climate modeling | foraminifera

The global climate system acts as a giant heat engine, working to redistribute the disproportionately large amount of incoming solar radiation per unit area at low latitudes to the high latitudes, where incident radiation is less. The latitudinal temperature gradient (LTG; here defined as the difference in sea-surface temperature [SST] between low [$<30^\circ$] and high [$>60^\circ$] latitudes) is one measure of this process and helps determine the strength of atmospheric circulation (1). The LTG is thus a key indicator for the behavior of the climate system in different background states and can serve as a test of how well climate models reproduce empirical records through time.

While global climate models have long predicted polar amplification—i.e., that high latitudes should experience greater warming than low latitudes in response to an increase in mean global temperature—the magnitude of this amplification has historically been much less than seen in most paleoclimate proxy records (2–7). Part of this discrepancy has arisen due to the challenges and limitations of surface-temperature proxies. For decades, proxy estimates of tropical SSTs in warm-climate states were similar to or lower than modern temperatures, predicting a greatly reduced LTG (8–11). It is now clear that this was due to pervasive recrystallization of foraminiferal $\delta^{18}\text{O}$, which biased the original SST signal and rendered most prior $\delta^{18}\text{O}$ -based SST estimates unreliable (12, 13). Recent compilations indicate higher tropical SSTs from warm intervals [>30 to 35°C (5, 6, 14, 15)], using a mix of organic (TEX_{86}) and inorganic temperature proxies ($\delta^{18}\text{O}$, Mg/Ca , and Δ_{47}) from exceptionally well-preserved samples. However, quantitative proxy estimates of LTGs in warm-climate states like the Eocene (4, 6, 7, 14, 16–18) and Cretaceous (5, 7, 19–25) remain relatively flat due, in part, to surprisingly warm high-latitude SSTs. While more recent climate models are better able to replicate polar amplification than previous-generation models (e.g., refs. 26–28), and some discrepancies relate to identifiable regional phenomena (29),

Significance

The temperature difference between low and high latitudes is one measure of the efficiency of the global climate system in redistributing heat and is used to test the ability of models to represent the climate system through time. Here, we show that the latitudinal temperature gradient has exhibited a consistent inverse relationship with global mean sea-surface temperature for at least the past 95 million years. Our results help reduce conflicts between climate models and empirical estimates of temperature and argue for a fundamental consistency in the dynamics of heat transport and radiative transfer across vastly different background states.

Author affiliations: ^aDepartment of Earth and Planetary Sciences, Yale University, New Haven, CT 06511; ^bDepartment of Earth, Atmospheric, and Planetary Sciences, Purdue University, West Lafayette, IN 47907; ^cDepartment of Geography, University College London, London WC1E 6BT, United Kingdom; ^dSchool of Ocean and Earth Science, National Oceanography Centre Southampton, University of Southampton, Southampton SO14 3ZH, United Kingdom; and ^eDepartment of Earth and Environmental Science, University of Michigan, Ann Arbor, MI 48109

Author contributions: D.E.G., M.H., C.L.O., G.N.I., R.P.A., C.J.P., and P.M.H. designed research; D.E.G., C.L.O., G.N.I., R.P.A., and C.J.P. performed research; D.E.G. contributed new reagents/analytic tools; D.E.G., C.L.O., and G.N.I. analyzed data; and D.E.G. wrote the paper.

The authors declare no competing interest.

This article is a PNAS Direct Submission.

Copyright © 2022 the Author(s). Published by PNAS. This article is distributed under Creative Commons Attribution-NonCommercial-NoDerivatives License 4.0 (CC BY-NC-ND).

¹To whom correspondence may be addressed. Email: daniel.gaskell@yale.edu.

This article contains supporting information online at <http://www.pnas.org/lookup/suppl/doi:10.1073/pnas.2111332119/-DCSupplemental>.

Published March 7, 2022.

temperature gradients predicted by models in extreme-climate states can remain up to $\sim 10^{\circ}\text{C}$ higher than those derived from these empirical compilations (5, 26, 27, 30–34).

Here, we revisit planktonic foraminifera $\delta^{18}\text{O}$ records to take advantage of their spatial and temporal coverage relative to other proxies and apply a number of approaches to overcome acknowledged limitations of the proxy. Using a global compilation of $\delta^{18}\text{O}$ measurements from surface-dwelling planktonic foraminifera, we generate a continuous, high-resolution record of low- and high-latitude SSTs, and the corresponding LTG, over the last 95 million years (My). We explore the sensitivity of LTG to changing boundary conditions, providing an emergent constraint for global climate models used to predict future climate states.

Approach

We infer low- and high-latitude SSTs for the last 95 My and provide a continuous record of LTGs and polar amplification during the Cenozoic and late Mesozoic using SSTs derived from planktonic foraminiferal $\delta^{18}\text{O}$ (*Methods*). To do so, we objectively screened a large compilation of planktonic foraminiferal $\delta^{18}\text{O}$ data (Fig. 1; 30,646 measurements, of which 4,238 were ultimately used to infer SSTs) and updated some of the methods used to infer SSTs.

The interpretation of foraminiferal $\delta^{18}\text{O}$ is complicated by changes in the $\delta^{18}\text{O}$ of seawater, as well as by biological vital effects and by diagenesis (35, 36). We applied methodological innovations to account for several previously underconstrained

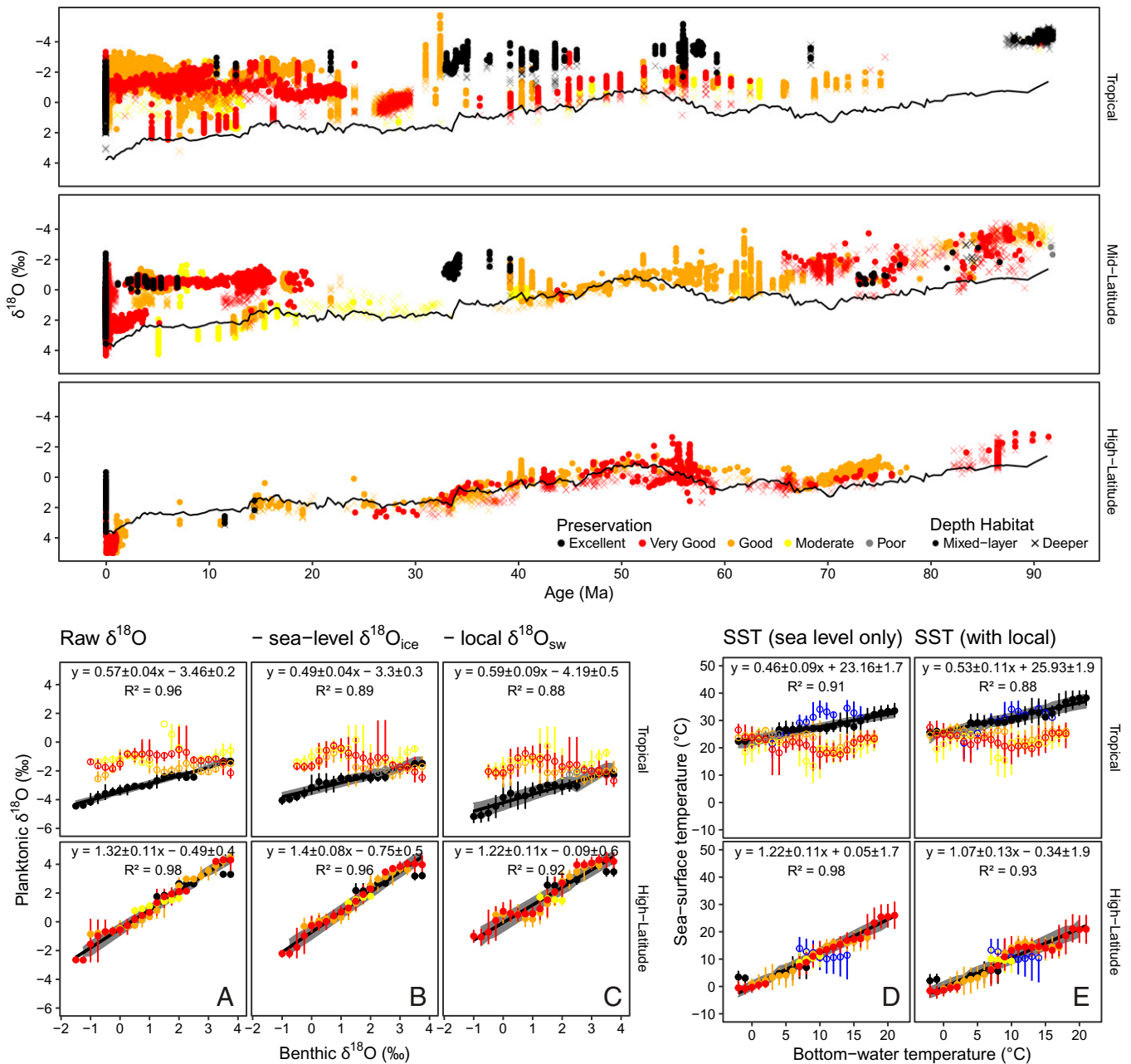


Fig. 1. (Upper) Raw $\delta^{18}\text{O}$ compilation (points) by age and latitude band, with colors indicating preservation and shapes indicating depth habitat. Black lines show the benthic $\delta^{18}\text{O}$ record. (Lower) All mixed-layer planktonic $\delta^{18}\text{O}$ data from the tropics and high southern latitudes, binned by benthic $\delta^{18}\text{O}$ or temperature and showing the series of corrections required to convert planktonic $\delta^{18}\text{O}$ to SSTs (as described in *Methods*). Clumped-isotope SSTs are shown in blue for comparison. Filled circles are used in calculating the least-squares regressions, while open circles are not used. Error bars represent 95% Monte Carlo CIs.

aspects of this system. To correct for local geographic variation in the $\delta^{18}\text{O}$ of seawater ($\delta^{18}\text{O}_{\text{sw}}$)—a major control on foraminiferal $\delta^{18}\text{O}$ that is usually unaccounted for or approximated using modern data (9, 37)—we used isotope-enabled runs of the Community Earth System Model (CESM) (38), aggregated into $10^\circ \times 10^\circ$ patches around each site to account for shifting current boundaries and interpolated across climate states to account for the climate dependence of $\delta^{18}\text{O}_{\text{sw}}$ gradients (*Methods* and *SI Appendix*). This method, which is similar in some respects to the method demonstrated by ref. 37, provides a spatially resolved and climate-sensitive update to the “classical” correction (9) and can be readily updated as new isotopically enabled general circulation model (GCM) runs become available. We additionally corrected for the vital effect of seawater $[\text{CO}_3^{2-}]$ on foraminiferal $\delta^{18}\text{O}$ (39–41). This effect is rarely considered when converting planktonic $\delta^{18}\text{O}$ to SST, despite longstanding evidence for its importance in both biological and inorganic calcification (e.g., refs. 39, 42, and 43). Finally, to work around the relative sparsity of exceptionally preserved planktonic foraminifera, we demonstrate and exploit the strong correlations between benthic and planktonic $\delta^{18}\text{O}$ (Fig. 1) to generate continuous estimates of SST from the comparatively data-dense record of benthic $\delta^{18}\text{O}$ (Fig. 2). These relationships are discussed in more detail in the following sections.

Results

Our data confirm that low-latitude ($\pm 0^\circ$ to 30° paleolatitude) planktonic foraminifera are most prone to diagenetic alteration (as in ref. 12), with the best-preserved specimens consistently recording the lowest $\delta^{18}\text{O}$ values relative to benthic $\delta^{18}\text{O}$ for the same time intervals and climate states (Fig. 1A). In contrast, at high latitudes ($>60^\circ$ S paleolatitude), planktonic $\delta^{18}\text{O}$ values closely track benthic $\delta^{18}\text{O}$ values, regardless of preservation status (Fig. 1A; $R^2 = 0.98$), likely due to the similarity between surface and bottom-water temperatures (BWTs) in the high latitudes. Our results for low latitudes are therefore based only on foraminifera with “Excellent” (glassy) preservation, while our results for the Southern Ocean use all preservation types.

After subsetting the data by preservation and correcting for other controls on foraminiferal $\delta^{18}\text{O}$, we found that low- and high-latitude SSTs covary with BWT with ordinary least-squares linear regression slopes of 0.53 ± 0.11 and 1.07 ± 0.13 , respectively (Fig. 1E; $R^2 = 0.88$ and 0.93 , respectively; slopes are unitless). By applying these regression relationships to the benthic $\delta^{18}\text{O}$ record, we inferred a continuous record of SSTs at low and high latitudes (Fig. 2). Regression-based high-latitude SSTs for the Southern Ocean are statistically indistinguishable from BWTs (multivariate distance of coefficients $D^2 = 1.52$, $P = 0.22$; Fig. 2). Predicted mean annual tropical

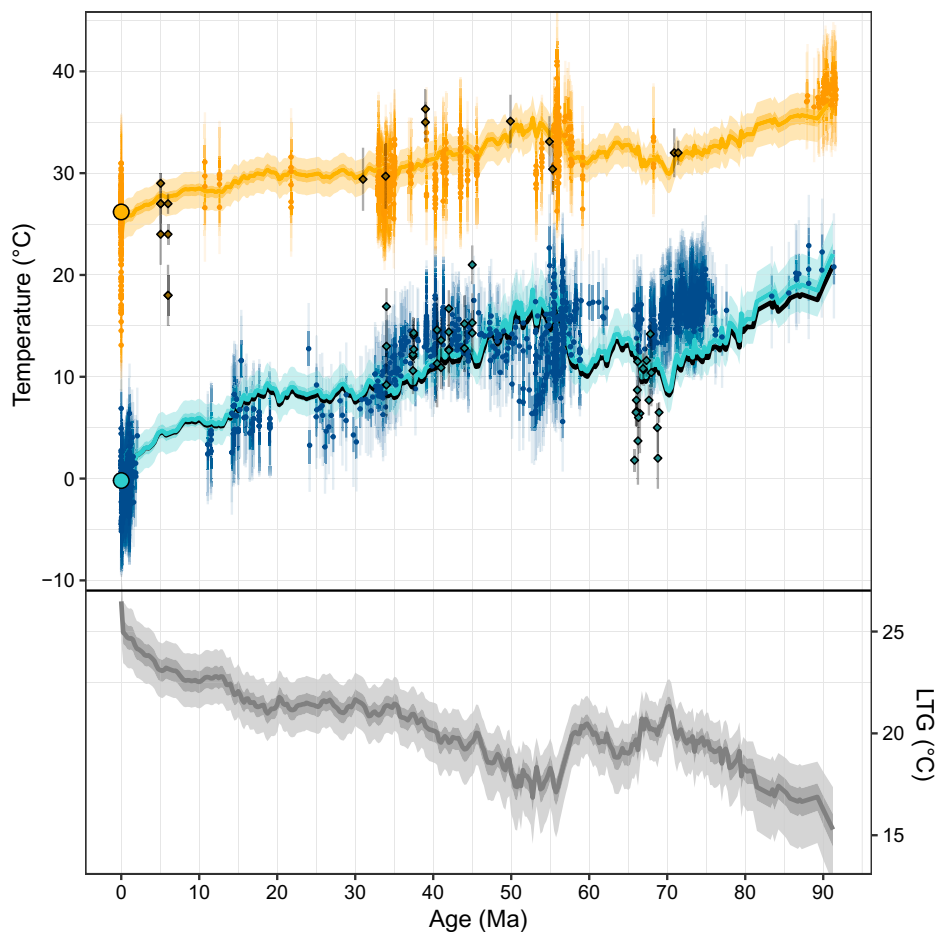


Fig. 2. $\delta^{18}\text{O}$ -based SSTs and LTGs over the last 95 My. (*Upper*) Points are individual $\delta^{18}\text{O}$ measurements converted to SST as in Fig. 1E. Bold lines are SSTs predicted from the benthic temperature curve using the regressions in Fig. 1E. For all symbols, yellow shades are tropical and blue shades are high-latitude, with dark and light bands indicating 50% and 95% Monte Carlo CIs, respectively. The benthic temperature curve is shown in black, partially covered by predicted high-latitude SST. Modern-day mean annual SSTs (large circles) and clumped-isotope SSTs (diamonds) are shown for comparison. (*Lower*) LTGs (grey line) obtained from the inferred continuous SSTs in *Upper*, with dark and light bands indicating 50% and 95% Monte Carlo CIs, respectively.

SSTs for the Early Eocene (56 to 47.8 millions of years ago [Ma]) range from 30.7 to 37.6 °C within 95% CIs. Maximum mean annual tropical SSTs of 33.8 to 38.6 °C occur at the start of our compilation in the Late Cretaceous (95% CI range at 91.8 Ma). Regression-based SST trends are consistent within error with individual SST measurements for 98% of tropical $\delta^{18}\text{O}$ data, 95% of high-latitude $\delta^{18}\text{O}$ data, 88% of tropical clumped-isotope data shown, 76% of high-latitude clumped-isotope data shown, and the modern mean values (two-sample t tests of points vs. prediction, $\alpha = 0.05$; Fig. 2). However, these regression-based trends predict colder high-latitude temperatures than clumped isotopes for the Eocene (mean residual = 2.5 °C) and slightly warmer high-latitude temperatures than clumped isotopes for the Late Cretaceous (mean residual = -3.6 °C). Predicted mean global SSTs for the Early Eocene Climatic Optimum (49.1 to 53.4 Ma) and latest Paleocene (57 Ma) are within error of estimates from ref. 44.

As indicated by the difference in slopes, the Southern Ocean is significantly more sensitive to changes in global temperatures than low latitudes (two-sample t test of slope distributions, $P < 0.01$), allowing us to estimate polar amplification through time (Fig. 3). Because the relationships between SSTs and BWTs are approximately linear (Fig. 1E), combining these regressions yields an inferred relationship between LTGs and BWTs that is also linear, i.e.,

$$\text{LTG} = -0.481(\pm 0.133) \times \text{BWT} + 25.25(\pm 1.68), \quad [1]$$

where LTG (in °C) is the difference in regression-predicted SST between low ($\pm 30^\circ$) and high ($>60^\circ\text{S}$) latitudes and BWT is the BWT in °C after the method of ref. 45. Errors are 95% Monte Carlo CIs based on all input uncertainties.

Expressed as a function of mean global SST (Fig. 3), this relationship is

$$\text{LTG} = -0.658(\pm 0.213) \times \text{GMSST} + 36.53(\pm 5.14), \quad [2]$$

where GMSST is mean global SST (in °C). Predicted LTG across the last 95 Ma spans 16.5 to 26.5 °C (Fig. 3), while predicted mean global SST spans 15.3 to 32.5 °C, over a benthic temperature range of -2.4 to 20.9 °C (45). Expressed as a polar amplification factor (PAF), this is

$$\frac{\Delta \text{SST}_{>60^\circ\text{S}}}{\Delta \text{SST}_{\text{mean}}} = 1.44(\pm 0.15). \quad [3]$$

Table 1 compares our results to prior proxy- and model-based estimates. Error terms are 95% Monte Carlo CIs from the error on all calibration steps.

We find that omitting the carbonate-ion effect correction results in SSTs that are 1.4 °C colder at 100 Ma, 1.1 °C colder at 40 Ma, and 0.6 °C colder at 10 Ma compared to the corrected values, with the difference decreasing over time as seawater $[\text{CO}_3^{2-}]$ increases toward modern values. The true error may be slightly larger, as the $[\text{CO}_3^{2-}]$ record appears to overestimate past seawater pH (ref. 46, figure 6) and consequently underestimate biases due to the carbonate-ion effect (41).

Discussion

Validating Models of Polar Amplification. The last 95 My span among the warmest “hothouse” and coldest “icehouse” climates known and thus much of the dynamic range of global temperatures that the Earth System has witnessed since the rise of complex animal life. Our study confirms and expands upon prior proxy work suggesting a negative relationship between LTG

Table 1. Estimates of the LTG to mean global SST relationship and equilibrium PAF, converted using the assumptions in this paper

	Slope	Intercept	PAF	Reference
This paper	-0.66 ± 0.21	36.53 ± 5.14	1.44 ± 0.15	This study
Proxy-based estimates				
Sijp compilation	-2.85	96.09	2.94	(4)
Cramwinckel compilation	-0.86	43.41	1.62 ± 0.16	(14)
Zhang compilation	-1.60	52.03	1.55	(7)
Model-based estimates (Pliocene)				
CESM2	-0.21	29.9	1.08	(70, 71)
EC-Earth3	-0.28	29.6	1.14	(72, 73)
GISS-E2	-0.26	31.4	1.01	(74, 75)
HadGEM3	-0.03	25.5	0.98	(76, 77)
NorESM	0.07	24.4	0.76	(78, 79)
Model-based estimates (Eocene)				
Model mean	-0.39	33.17	1.27 ± 0.06	(27)
CESMv1.2	-0.37	31.07	1.25	(27)
COSMOS	0.11	22.70	0.92	(27)
GFDL	-0.30	30.00	1.20	(27)
HadCM3	-0.25	30.58	1.17	(27)
IPSL	-0.24	30.25	1.16	(27)
NorESM	-0.75	41.5	1.51	(27)
Model-based estimates (Cretaceous/General)				
100-My HadCM3	-0.21	29.4	1.05	(56)
Maastrichtian CCSM4	-0.31	32.0	1.18	(80)

The 95% CIs on regressions are provided where possible. CCSM4, Community Climate System Model Version 4; COSMOS, Community Earth System Models; EC-Earth3, European Community Earth System Model 3; GFDL, Geophysical Fluid Dynamics Laboratory model; GISS-E2, Goddard Institute for Space Studies Model E2; HadGEM3, Hadley Centre Global Environment Model Version 3; IPSL, Institut Pierre-Simon Laplace model.

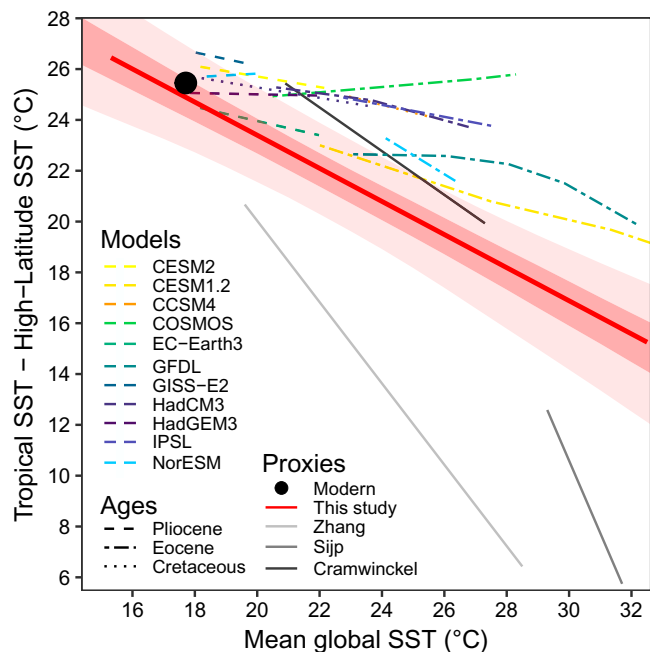


Fig. 3. Calculated relationships between the LTG and global mean SST. The red line shows our results, with dark and light bands indicating 50% and 95% Monte Carlo CIs, respectively; other lines show linear least-squares regressions of prior estimates. References for prior estimates are given in Table 1. CCSM4, Community Climate System Model Version 4; COSMOS, Community Earth System Models; EC-Earth3, European Community Earth System Model 3; GFDL, Geophysical Fluid Dynamics Laboratory model; GISS-E2, Goddard Institute for Space Studies Model E2; HadGEM3, Hadley Centre Global Environment Model Version 3; IPSL, Institut Pierre-Simon Laplace model.

and global SST, with the lowest LTGs during intervals with the highest global SSTs (Fig. 3, this study, and refs. 4, 7, and 14). However, prior compilations have disagreed dramatically in their estimates of the slope and intercept of this relationship (Fig. 3), primarily due to differences in the input datasets used to calculate high-latitude SSTs. Prior compilations that include high-latitude SSTs from TEX_{86} and/or Mg/Ca yield lower Eocene LTGs (~ 6 to 14°C ; refs. 4 and 7) than those predicted by a coordinated set of model simulations for the same time period (Fig. 3, Table 1, and ref. 27). High-latitude SSTs inferred via TEX_{86} also yield low LTGs during the Cretaceous (21–24). In contrast, using BWTs to reconstruct high-latitude SSTs yields higher LTGs in warm-climate states ($>20^\circ\text{C}$; refs. 6 and 14), in better agreement with models (Fig. 3). This latter approach assumes that BWTs are able to approximate high-latitude SSTs, which our results support (Fig. 1E).

Our results exhibit a shallower slope than existing proxy-based relationships and more closely resemble the global SST–LTG relationship predicted by models (Fig. 3), although discrepancies remain, especially in warmer-climate states. Of the simulations shown here (27), the Norwegian Earth System Model (NorESM) and CESM (version 1) families of models are best able to reproduce our inferred polar amplification, consistent with prior work (26), although predicted LTGs in the warmest-climate states remain higher than our results. Other model families predict even higher LTGs and even less polar amplification than our results. This improved concordance between proxies and models supports the realism of the heat-transport dynamics and polar feedbacks in the current generation of climate models.

Covariance of LTGs with Global Climate: Evidence and Limitations. The observed correlation between planktonic and benthic $\delta^{18}\text{O}$ suggests a fundamental consistency in the

dynamics of latitudinal heat transport and polar amplification across vastly different background states of continental configuration, ocean circulation, and ice volume. Our reconstruction treats the relationship between SSTs and BWTs as linear, an assumption that appears to hold across the majority of the past 95 My. However, examination of the regression residuals through time (Fig. 4) highlights several intervals between the Late Cretaceous and the Late Eocene where SSTs may have diverged from this expectation by 5°C or more. This is primarily the case in the high southern latitudes, where $\delta^{18}\text{O}$ -derived SSTs from the Southern Ocean exhibit a less consistent relationship with BWTs and clumped isotope-derived temperatures than do $\delta^{18}\text{O}$ -derived SSTs from the tropics (Fig. 4; SD of residuals in the tropics before 30 Ma = 2.0°C and at high latitudes = 3.6°C). These residuals are evidently large enough to overcome the effects of diagenetic overprinting, which would otherwise tend to pull high-latitude SSTs toward BWTs.

It is not presently known whether these intervals represent genuine deviations from linearity or simply systematic biases affecting the individual SSTs, but several lines of evidence argue for the latter option. One potential source of bias is local variation in seawater $\delta^{18}\text{O}$ in the Southern Ocean, where—prior to the opening of the Drake Passage—models predict 1.3 to 3.4 times greater variability in $\delta^{18}\text{O}_{\text{sw}}$ than in the tropical Pacific (data from ref. 47). There is similarly a strong likelihood of spatial bias due to sites recording hotter or colder local conditions than the zonal mean. Evidence for this can be found in our model results, where spatial SST biases predicted by CESM (i.e., the difference between modeled SSTs for each site and the corresponding modeled zonal mean SST for the same age) can explain 49.4% of the variability in the high-latitude residuals shown in Fig. 4 and 12.9% of the variability in the low-latitude residuals (R^2 of ordinary least-squares linear regressions; *SI Appendix*, section 1.12). $\delta^{18}\text{O}$ -based SSTs from planktonic foraminifera may also be biased by shifting seasonality and depth habitats, either to best exploit their environment or to remain within their preferred thermal niche (48). Our SST calibration implicitly accounts for these factors under modern conditions (49), and our analysis spans multiple complete faunal turnovers, so small-scale changes in depth habitat are unlikely to significantly affect our estimates of PAF, although they may be observable on shorter (<10 My) timescales. The question of seasonality is more complex. In the tropics, foraminifera fluxes most frequently peak in late autumn (50), when temperatures are close to (or slightly above) mean annual SST (e.g., ref. 51), with seasonality decreasing as mean temperature increases (50). In the high latitudes, seasonality in plankton communities is largely driven by fundamental geographic limitations on light and nutrient availability (52), yielding one or two peaks in foraminifera flux in the spring and fall (50). While it is possible for changing climate conditions to alter the seasonal timing of foraminifera fluxes, niche-tracking tends to dampen, rather than amplify, the effects of seasonality on proxies (48), and fundamental constraints on plankton growth (such as the lack of light during high-latitude winters) decrease the likelihood that peak foraminifera production could have shifted to occur during seasonal extremes. It is therefore unlikely that either our high- or low-latitude data are strongly biased by changes in the seasonality of foraminifera production relative to the modern. However, other species-specific trends may explain some of the most striking divergences seen in Fig. 4. In particular, the lowest SSTs for the Late Paleocene and Early Eocene (60 to 48 Ma) are associated with just one species, *Subbotina triangularis*, while other species from the same sites yield SSTs in better agreement with

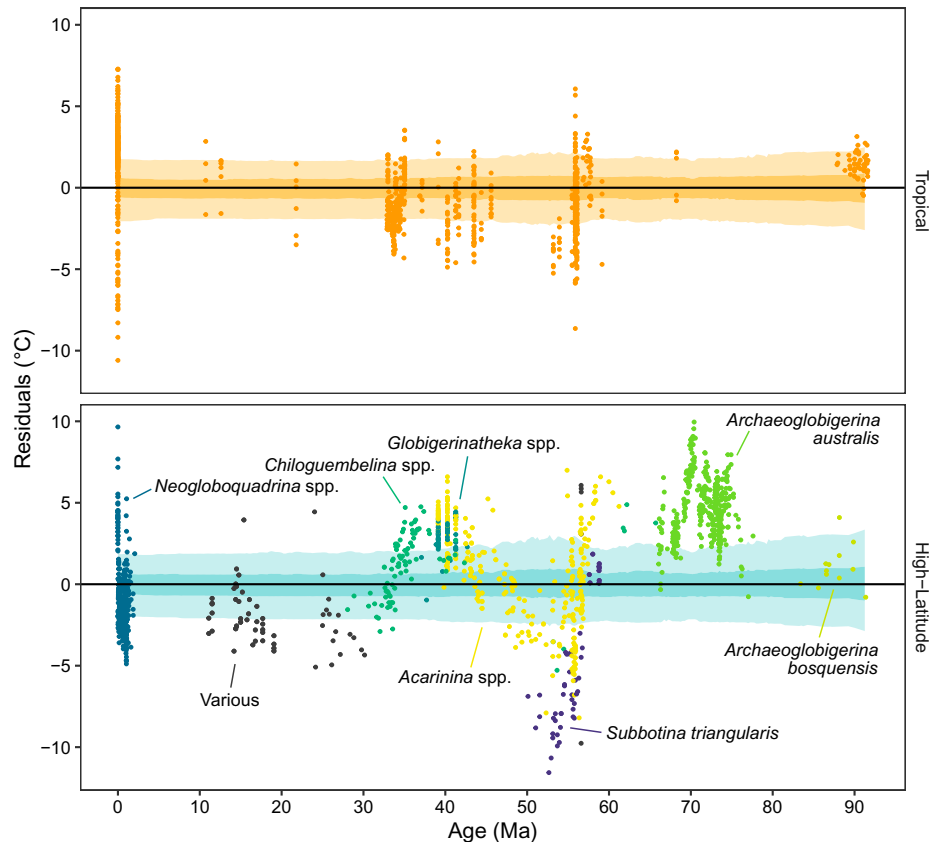


Fig. 4. Residuals of individual measurements (points) from our continuous temperature reconstruction (horizontal axes, with dark and light bands indicating 50% and 95% Monte Carlo CIs, respectively). Colors in *Lower* indicate species, as indicated.

our curve (Fig. 4). Ecological assessments differ on whether *S. triangularis* actually lived within the mixed layer (53) or occupied a deeper niche than co-occurring species (54). Similarly, the data from the late Campanian and Maastrichtian (74 to 66 Ma) yielding higher SSTs than our curve represent only one species, *Archaeoglobigerina australis*, at one site, Ocean Drilling Program 690 (Fig. 4). The foregoing examples suggest that the deviations from linearity observed in Fig. 4 may be the result of systematic biases in the temperature reconstructions, rather than genuine nonlinearities in the climate system.

While there is a strong need for more data from well-preserved foraminifera across several time intervals, particularly the Neogene and the Late Cretaceous (Fig. 2), it is important to note that our method does not rely on data coverage across time, but rather across climate states (Fig. 1). Additional data for the Neogene and Late Cretaceous would, however, help to test the validity of our hypotheses.

While prior analyses have often assumed that $\delta^{18}\text{O}$ -derived SSTs were more reliable at high latitudes than in the tropics due to cooler temperatures and the close relationship between high-latitude SSTs and BWT (e.g., refs. 12 and 14), our results suggest the opposite. The sensitivity of foraminiferal $\delta^{18}\text{O}$ to local $\delta^{18}\text{O}_{\text{sw}}$ also highlights the utility of the measurement-regression residuals (Fig. 4) as a tool for understanding Southern Ocean hydrography.

Internal Consistency of Climate Models. Because our method of reconstructing surface $\delta^{18}\text{O}_{\text{sw}}$ relies on GCM outputs, our proxy-inferred LTG estimates are not fully independent of the GCMs to which we compare them in Fig. 3. Therefore, our results can be more appropriately thought of as a test of the internal consistency of the model physics and of the consistency of the model

physics with the available data, rather than as a wholly independent validation dataset. The strengths and limitations of this approach can be seen through a qualitative examination of alternate scenarios. If the $\delta^{18}\text{O}_{\text{sw}}$ gradient were significantly more climate-sensitive than predicted by the model, inferred high-latitude SSTs would fall out of agreement with BWTs, and the discrepancy between the $\delta^{18}\text{O}$ -predicted LTGs and the GCM-predicted LTGs would increase. Conversely, if the $\delta^{18}\text{O}_{\text{sw}}$ gradient were significantly less climate-sensitive than predicted by the model, inferred mean annual Southern Ocean SSTs would become colder than BWTs under the warmest-climate states, which is physically improbable. The consistency between the $\delta^{18}\text{O}$ temperatures and the GCM-simulated temperatures supports the accuracy of the simulation as a whole. This caveat also applies primarily to only one model family (CESM), and other isotope-enabled simulations [e.g., the Hadley Centre Coupled Model, version 3 (HadCM3) for the Eocene (55)] yield similar predicted $\delta^{18}\text{O}_{\text{sw}}$ trends (*SI Appendix, Fig. S3*), despite large differences in modeled LTGs. Our finding that high-latitude SST closely tracks BWTs is consistent with the behavior of HadCM3 over the Phanerozoic (ref. 56, figure 6).

Even without correcting for the climate-state dependence of $\delta^{18}\text{O}_{\text{sw}}$, we would still infer lower LTGs in warmer-climate states because the underlying data show a steeper slope in the planktic:benthic $\delta^{18}\text{O}$ relationship at high latitudes than at low latitudes (slope 1.32 vs. 0.57; Fig. 1A).

Conclusions

Here, we identify a consistent covariance between benthic and planktonic foraminifera $\delta^{18}\text{O}$ across different latitudinal bands and exploit this relationship to infer a high-resolution SST

record at high and low latitudes for the last 95 My. To do so, we have developed estimates of site-specific $\delta^{18}\text{O}_{\text{sw}}$ by interpolating across isotope-enabled global climate models. Our approach fills in sparse data coverage and allows us to examine the evolution of LTGs over a wide range of climate states. In these records, the lowest LTGs occur during the intervals with the highest global SSTs (LTG = 26.5°C for a mean global SST of 15.3°C, and LTG = 15.3°C for a mean global SST of 32.5°C), with an apparently consistent relationship between sea-surface LTGs and global temperature, regardless of changing boundary conditions like continental configuration or global ice volume. Our estimates are in closer agreement with some numerical climate models than previous proxy-based estimates, providing confirmation that these models can simulate climate states different from the modern and supporting their use in forecasting future climate.

Methods

We compiled planktonic foraminifera $\delta^{18}\text{O}$ measurements from published sources (Dataset S1 and references in *SI Appendix, section 1.1*). We assessed paleolatitude and paleo-longitude using GPlates (57), assigned sites to 30° latitudinal bands, and qualitatively assigned each measurement to one of five preservation categories (Excellent, Very Good, Good, Moderate, or Poor) used in published work, with Excellent generally indicating glassy preservation (i.e., minimal diagenetic alteration, suitable for estimation of absolute temperature; ref. 58). Only species and genera identified as mixed-layer-dwelling in the literature were included in our primary analysis. High-latitude data were restricted to the Southern Hemisphere due to the greater heterogeneity of seawater $\delta^{18}\text{O}$ at high northern latitudes, which greatly increases the uncertainty of SST conversions (*SI Appendix, Figs. S3 and S10*). Midlatitudes were likewise excluded due to their comparative lack of high-quality data (Fig. 1; see also *SI Appendix, Fig. S20*). For benthic $\delta^{18}\text{O}$ and BWTs, we used the records and temperature estimates of ref. 45, smoothed to 250 kilo-annum, and extended into the Late Cretaceous with additional sources from the literature (references in *SI Appendix, section 1.1*).

To convert $\delta^{18}\text{O}$ to SST, we corrected for: 1) the carbonate-ion effect (39) using the seawater $[\text{CO}_3^{2-}]$ curve of ref. 46 and the mean carbonate-ion effect of four species of planktonic foraminifera (40); 2) global variations in the $\delta^{18}\text{O}$ of seawater due to ice cover by subtracting seawater $\delta^{18}\text{O}$ inferred by ref. 45 (Fig. 1B); and 3) local seawater $\delta^{18}\text{O}$ by subtracting modern seawater $\delta^{18}\text{O}$ [Pliocene to modern: median of 10° × 10° patches (59)] or using modeled seawater $\delta^{18}\text{O}$ (Cretaceous to Miocene: median of 10° × 10° patches) from isotope-enabled runs of the CESM (Fig. 1C). To infer local seawater $\delta^{18}\text{O}$ from the Cretaceous–Eocene, we used published CESM runs with Eocene paleogeography (47); for data from the Oligocene–Miocene, we used our own isotope-enabled CESM runs with Miocene paleogeography, published here (*SI Appendix, section 1.9*). We accounted for uncertainty in the reconstruction of site location, current boundaries, and evolving oceanography on local seawater $\delta^{18}\text{O}$ estimates by averaging seawater $\delta^{18}\text{O}$ in relatively large spatial patches (10° × 10°) and interpolating these patches between model runs using natural splines and the high-latitude temperature predicted by each model run (*SI Appendix, section 1.4*). (Local seawater corrections for each site in 5-My time steps are provided in Dataset S3; a general polynomial approximation is given as *SI Appendix, Eq. S9*.) Corrected $\delta^{18}\text{O}$ values were then converted to SSTs by using the pooled bayfox Bayesian calibration (49). Our temperature estimates are robust to uncertainties in species calibrations, with calculations based on inorganic precipitates differing from bayfox-based temperature reconstructions by <2°C (*SI Appendix, Fig. S6*).

To select preservation criteria for low and high latitudes and to infer planktonic SSTs over sparsely sampled intervals, we first calculated the relationship between planktonic and benthic $\delta^{18}\text{O}$ within different preservation states by binning planktonic $\delta^{18}\text{O}$ values into 0.25‰ intervals of the benthic $\delta^{18}\text{O}$ values corresponding to their ages and fitting ordinary least-squares linear regressions to the bin medians (Fig. 1A). At low latitudes, planktonic foraminifera with Excellent preservation exhibited the lowest $\delta^{18}\text{O}$ values, indicating the least diagenetic overprinting with benthic values, while they simultaneously showed the strongest covariance with benthic $\delta^{18}\text{O}$ compared to other preservation states (Fig. 1A). At high latitudes, all planktonic foraminifera exhibited a similar covariance with benthic foraminifera, regardless of preservation (Fig. 1A). Based on these results, we continued our analysis using only SSTs derived from Excellent foraminifera in low latitudes, but all foraminiferal-based SSTs in high latitudes. As before, we calculated the relationship between surface temperatures and BWTs (Fig. 1D and E) by binning calculated SSTs into 1°C intervals of benthic temperature. The resulting linear regressions were then used to infer low- and high-latitude SSTs across our entire interval of study using the benthic record of BWT (Fig. 2).

We performed Monte Carlo error estimation on all calculations by randomizing all parameters within distributions defined by 1) the published estimated error on $[\text{CO}_3^{2-}]$ and ice cover (*SI Appendix, section 1.7*); 2) the SD of $\delta^{18}\text{O}$ within each 10° × 10° patch in our CESM runs; 3) the uncertainty distribution of each SST conversion estimated by bayfox (49); 4) the SD of referenced slopes for the carbonate-ion effect; and 5) a temporal error term in Fig. 1 of ±1 bin (0.25‰, or 1°C). To account for the effect of systematic error on bin medians (such as the possibility that seawater $\delta^{18}\text{O}$ could be offset in the same direction for an entire record), random offsets on $[\text{CO}_3^{2-}]$ and seawater $\delta^{18}\text{O}$ were treated on a record-by-record basis within each Monte Carlo run. Initial data exploration also indicated that reconstructions of LTGs were potentially sensitive to the inclusion or exclusion of particular datasets. To account for this data-coverage effect, we also bootstrapped which measurements were included in our regressions and propagated this error through to the calculations of uncertainty on latitudinal gradients and polar amplification.

We tested $\delta^{18}\text{O}$ -based SST reconstructions with modern SSTs from GLODAPv2 (60, 61) and clumped-isotope SST estimates from the literature (6, 62–66). Our clumped-isotope compilation excludes poorly preserved specimens (e.g., ref. 67) and samples from known thermocline dwellers (e.g., ref. 68). For Fig. 3 and Eq. 3, mean global SST was estimated from low- and high-latitude SSTs by area-weighting on a sphere (*SI Appendix, Eq. S5*, following ref. 69).

Data Availability. Data tables compiling previously published data with calculated statistics data are included in *SI Appendix*. Previously published data were used for this work (listed in *SI Appendix*).

ACKNOWLEDGMENTS. M.H. acknowledges support by NSF P2C2 Award 1602905. C.L.O. acknowledges the support of a Yale Institute for Biospheric Studies Donnelley Postdoctoral Environmental Fellowship and NSF P2C2 Award 1602557. G.N.I. acknowledges support by Royal Society Dorothy Hodgkin Fellowship DHR1191178. R.P.A. and C.J.P. acknowledge support through Heising Simon Foundation Award 2016-05 and NSF Award 1550134. P.M.H. acknowledges support through a Sloan Ocean Fellowship and NSF P2C2 Award 1602557. We acknowledge the World Climate Research Programme, the Earth System Grid Federation (ESGF), and the participating climate-modeling groups of Coupled Model Intercomparison Project 6 (CMIP6) for producing, archiving, and promoting many of the model outputs used for this paper, as well as the multiple funding agencies that support CMIP6 and ESGF. This research used data provided by the International Ocean Discovery Program. We also thank two anonymous reviewers for comments that greatly improved this manuscript.

1. C. Karamperidou, F. Cioffi, U. Lall, Surface temperature gradients as diagnostic indicators of midlatitude circulation dynamics. *J. Clim.* **25**, 4154–4171 (2012).
2. A. P. Ballantyne *et al.*, Significantly warmer Arctic surface temperatures during the Pliocene indicated by multiple independent proxies. *Geology* **38**, 603–606 (2010).
3. H. J. Dowsett *et al.*, Assessing confidence in Pliocene sea surface temperatures to evaluate predictive models. *Nat. Clim. Chang.* **2**, 365–371 (2012).
4. W. P. Sijp *et al.*, The role of ocean gateways on cooling climate on long time scales. *Glob. Planet. Change* **119**, 1–22 (2014).
5. C. L. O'Brien *et al.*, Cretaceous sea-surface temperature evolution: Constraints from TEX86 and planktonic foraminiferal oxygen isotopes. *Earth Sci. Rev.* **172**, 224–247 (2017).

6. D. Evans *et al.*, Eocene greenhouse climate revealed by coupled clumped isotope-Mg/Ca thermometry. *Proc. Natl. Acad. Sci. U.S.A.* **115**, 1174–1179 (2018).
7. L. Zhang, W. W. Hay, C. Wang, X. Gu, The evolution of latitudinal temperature gradients from the latest Cretaceous through the present. *Earth Sci. Rev.* **189**, 147–158 (2019).
8. L. A. Frakes, J.-L. Probst, W. Ludwig, Latitudinal distribution of paleotemperature on land and sea from early Cretaceous to middle Miocene. *Sci. Terre Planètes Comptes Rendus Académie Sci.* **318**, 1209–1218 (1994).
9. J. C. Zachos, L. D. Stott, K. C. Lohmann, Evolution of Early Cenozoic marine temperatures. *Paleoceanography* **9**, 353–387 (1994).

10. T. J. Bralower *et al.*, Late Paleocene to Eocene paleoceanography of the equatorial Pacific Ocean: Stable isotopes recorded at Ocean Drilling Program Site 865, Allison Guyot. *Paleoceanography* **10**, 841–865 (1995).
11. B. T. Huber, D. A. Hodell, C. P. Hamilton, Middle–Late Cretaceous climate of the southern high latitudes: Stable isotopic evidence for minimal equator-to-pole thermal gradients. *Geol. Soc. Am. Bull.* **107**, 1164–1191 (1995).
12. P. N. Pearson *et al.*, Warm tropical sea surface temperatures in the Late Cretaceous and Eocene epochs. *Nature* **413**, 481–487 (2001).
13. R. D. Norris, K. L. Bice, E. A. Magno, P. A. Wilson, Jiggling the tropical thermostat in the Cretaceous hothouse. *Geology* **30**, 299–302 (2002).
14. M. J. Cramwinckel *et al.*, Synchronous tropical and polar temperature evolution in the Eocene. *Nature* **559**, 382–386 (2018).
15. M. Huber, Climate change. A hotter greenhouse? *Science* **321**, 353–354 (2008).
16. A. Sluijs *et al.*, Expedition 302 Scientists, Subtropical Arctic Ocean temperatures during the Paleocene/Eocene thermal maximum. *Nature* **441**, 610–613 (2006).
17. G. N. Inglis *et al.*, Descent toward the Icehouse: Eocene sea surface cooling inferred from GDGT distributions. *Paleoceanography* **30**, 1000–1020 (2015).
18. C. J. Hollis *et al.*, The DeepMIP contribution to PMIP4: Methodologies for selection, compilation and analysis of latest Paleocene and early Eocene climate proxy data, incorporating version 0.1 of the DeepMIP database. *Geosci. Model Dev.* **12**, 3149–3206 (2019).
19. R. Amiot *et al.*, Latitudinal temperature gradient during the Cretaceous Upper Campanian–Middle Maastrichtian: $\delta^{18}\text{O}$ record of continental vertebrates. *Earth Planet. Sci. Lett.* **226**, 255–272 (2004).
20. J. S. Sinninghe Damsté, E. C. van Bentum, G.-J. Reichart, J. Pross, S. Schouten, A CO_2 decrease-driven cooling and increased latitudinal temperature gradient during the mid-Cretaceous Oceanic Anoxic Event 2. *Earth Planet. Sci. Lett.* **293**, 97–103 (2010).
21. K. Littler, S. A. Robinson, P. R. Bown, A. J. Nederbragt, R. D. Pancost, High sea-surface temperatures during the Early Cretaceous Epoch. *Nat. Geosci.* **4**, 169–172 (2011).
22. B. D. A. Naafs, R. D. Pancost, Sea-surface temperature evolution across Aptian Oceanic Anoxic Event 1a. *Geology* **44**, 959–962 (2016).
23. L. K. O'Connor *et al.*, Late Cretaceous temperature evolution of the southern high latitudes: A TEX₈₆ perspective. *Paleoceanogr. Paleoclimatol.* **34**, 436–454 (2019).
24. M. L. Vickers, D. Bajnai, G. D. Price, J. Linckens, J. Fiebig, Southern high-latitude warmth during the Jurassic–Cretaceous: New evidence from clumped isotope thermometry. *Geology* **47**, 724–728 (2019).
25. G. D. Price, D. Bajnai, J. Fiebig, Carbonate clumped isotope evidence for latitudinal seawater temperature gradients and the oxygen isotope composition of Early Cretaceous seas. *Palaeogeogr. Palaeoclimatol. Palaeoecol.* **552**, 109777 (2020).
26. J. Zhu, C. J. Poulsen, J. E. Tierney, Simulation of Eocene extreme warmth and high climate sensitivity through cloud feedbacks. *Sci. Adv.* **5**, eaax1874 (2019).
27. D. J. Lunt *et al.*, DeepMIP: Model intercomparison of Early Eocene Climatic Optimum (EECO) large-scale climate features and comparison with proxy data. *Clim. Past* **17**, 203–227 (2021).
28. A. M. Haywood *et al.*, The Pliocene Model Intercomparison Project Phase 2: Large-scale climate features and climate sensitivity. *Clim. Past* **16**, 2095–2123 (2020).
29. E. L. McLymont *et al.*, Lessons from a high- CO_2 world: An ocean view from ~3 million years ago. *Clim. Past* **16**, 1599–1615 (2020).
30. D. J. Lunt *et al.*, A model-data comparison for a multi-model ensemble of early Eocene atmosphere–ocean simulations: EoMIP. *Clim. Past* **8**, 1717–1736 (2012).
31. A. Goldner, N. Herold, M. Huber, The challenge of simulating the warmth of the Mid-Miocene Climatic Optimum in CESM1. *Clim. Past* **10**, 523–536 (2014).
32. Y. Donnadieu, E. Pucéat, M. Moiroud, F. Guillocheau, J.-F. Deconinck, A better-ventilated ocean triggered by Late Cretaceous changes in continental configuration. *Nat. Commun.* **7**, 10316 (2016).
33. J. E. Tierney, A. M. Haywood, R. Feng, T. Bhattacharya, B. L. Otto-Bliesner, Pliocene warmth consistent with greenhouse gas forcing. *Geophys. Res. Lett.* **46**, 9136–9144 (2019).
34. N. J. Burls *et al.*, Simulating Miocene warmth: Insights from an opportunistic multi-model ensemble (MioMIP1). *Paleoceanogr. Paleoclimatol.* **35**, e2020PA004054 (2021).
35. A. C. Ravelo, C. Hillaire-Marcel, “The use of oxygen and carbon isotopes of foraminifera in paleoceanography” in *Proxies in Late Cenozoic Paleoclimatology*, C. Hillaire-Marcel, A. de Vernal, Eds (Developments in Marine Geology, Elsevier, Amsterdam, 2007), vol. 1, pp. 735–764.
36. P. N. Pearson, Oxygen isotopes in foraminifera: Overview and historical review. *Paleontol. Soc. Pap.* **18**, 1–38 (2012).
37. J. Zhou, C. J. Poulsen, D. Pollard, T. S. White, Simulation of modern and middle Cretaceous marine $\delta^{18}\text{O}$ with an ocean-atmosphere general circulation model. *Paleoceanography* **23**, PA3223 (2008).
38. E. Brady *et al.*, The connected isotopic water cycle in the Community Earth System Model version 1. *J. Adv. Model. Earth Syst.* **11**, 2547–2566 (2019).
39. H. J. Spero, J. Bijma, D. W. Lea, B. E. Bemis, Effect of seawater carbonate concentration on foraminiferal carbon and oxygen isotopes. *Nature* **390**, 497–500 (1997).
40. H. J. Spero, J. Bijma, D. W. Lea, A. D. Russell, “Deconvolving glacial ocean carbonate chemistry from the planktonic foraminifera carbon isotope record” in *Reconstructing Ocean History: A Window into the Future*, F. Abrantes, A. C. Mix, Eds. (Springer, Boston, 1999), pp. 329–342.
41. J. Bijma, H. J. Spero, D. W. Lea, “Reassessing foraminiferal stable isotope geochemistry: impact of the oceanic carbonate system (experimental results)” in *Use of Proxies in Paleoclimatology: Examples from the South Atlantic*, D. G. Fischer, P. D. G. Weyer, Eds. (Springer, Berlin Heidelberg, 1999), pp. 489–512.
42. J. M. McCrea, On the isotopic chemistry of carbonates and a paleotemperature scale. *J. Chem. Phys.* **18**, 849–857 (1950).
43. P. Ziveri, S. Thoms, I. Probert, M. Geisen, G. Langer, A universal carbonate ion effect on stable oxygen isotope ratios in unicellular planktonic calcifying organisms. *Biogeosciences* **9**, 1025–1032 (2012).
44. G. N. Inglis *et al.*, Global mean surface temperature and climate sensitivity of the Early Eocene Climatic Optimum (EECO), Paleocene–Eocene Thermal Maximum (PETM), and latest Paleocene. *Clim. Past* **16**, 1953–1968 (2020).
45. K. G. Miller *et al.*, Cenozoic sea-level and cryospheric evolution from deep-sea geochemical and continental margin records. *Sci. Adv.* **6**, eaaz1346 (2020).
46. R. E. Zeebe, T. Tyrrell, History of carbonate ion concentration over the last 100 million years II: Revised calculations and new data. *Geochim. Cosmochim. Acta* **257**, 373–392 (2019).
47. J. Zhu *et al.*, Simulation of early Eocene water isotopes using an Earth system model and its implication for past climate reconstruction. *Earth Planet. Sci. Lett.* **537**, 116164 (2020).
48. L. Jonkers, M. Kucera, Quantifying the effect of seasonal and vertical habitat tracking on planktonic foraminifera proxies. *Clim. Past* **13**, 573–586 (2017).
49. S. B. Malevich, L. Vetter, J. E. Tierney, Global core top calibration of $\delta^{18}\text{O}$ in planktic foraminifera to sea surface temperature. *Paleoceanogr. Paleoclimatol.* **34**, 1292–1315 (2019).
50. L. Jonkers, M. Kucera, Global analysis of seasonality in the shell flux of extant planktonic Foraminifera. *Biogeosciences* **12**, 1733–1752 (2015).
51. M. Alexander, H. Kilbourne, J. Nye, Climate variability during warm and cold phases of the Atlantic Multidecadal Oscillation (AMO) 1871–2008. *J. Mar. Syst.* **133**, 14–26 (2014).
52. A. R. Longhurst, *Ecological Geography of the Sea* (Academic Press, New York, 1998).
53. T. Aze *et al.*, A phylogeny of Cenozoic macroforiferate planktonic foraminifera from fossil data. *Biol. Rev. Camb. Philos. Soc.* **86**, 900–927 (2011).
54. R. K. Olsson, W. A. Berggren, C. Hemleben, B. T. Huber, *Atlas of Paleocene Planktonic Foraminifera* (Smithsonian Contributions to Paleobiology, Smithsonian Institution Press, Washington, DC, 1999), vol. 85.
55. J. Tindall *et al.*, Modelling the oxygen isotope distribution of ancient seawater using a coupled ocean–atmosphere GCM: Implications for reconstructing early Eocene climate. *Earth Planet. Sci. Lett.* **292**, 265–273 (2010).
56. P. J. Valdes, C. R. Scotese, D. J. Lunt, Deep ocean temperatures through time. *Clim. Past* **17**, 1483–1506 (2021).
57. R. D. Müller *et al.*, GPlates: Building a virtual Earth through deep time. *Geochem. Geophys. Geosyst.* **19**, 2243–2261 (2018).
58. P. F. Sexton, P. A. Wilson, P. N. Pearson, Microstructural and geochemical perspectives on planktic foraminiferal preservation: “Glassy” versus “Frosty.” *Geochem. Geophys. Geosyst.* **7**, Q12P19 (2006).
59. A. N. LeGrande, G. A. Schmidt, Global gridded data set of the oxygen isotopic composition in seawater. *Geophys. Res. Lett.* **33**, L12604 (2006).
60. A. Olsen *et al.*, The Global Ocean Data Analysis Project version 2 (GLODAPv2)—An internally consistent data product for the world ocean. *Earth Syst. Sci. Data* **8**, 297–323 (2016).
61. R. M. Key *et al.*, Global Ocean Data Analysis Project, Version 2 (GLODAPv2). Carbon Dioxide Information Analysis Center, Oak Ridge National Laboratory (2015).
62. P. M. J. Douglas *et al.*, Pronounced zonal heterogeneity in Eocene southern high-latitude sea surface temperatures. *Proc. Natl. Acad. Sci. U.S.A.* **111**, 6582–6587 (2014).
63. A. J. Drury, C. M. John, Exploring the potential of clumped isotope thermometry on coccolith-rich sediments as a sea surface temperature proxy. *Geochem. Geophys. Geosyst.* **17**, 4092–4104 (2016).
64. K. W. Meyer, S. V. Petersen, K. C. Lohmann, I. Z. Winkelstern, Climate of the Late Cretaceous North American Gulf and Atlantic Coasts. *Cretac. Res.* **89**, 160–173 (2018).
65. S. V. Petersen, A. Dutton, K. C. Lohmann, End-Cretaceous extinction in Antarctica linked to both Deccan volcanism and meteorite impact via climate change. *Nat. Commun.* **7**, 12079 (2016).
66. S. V. Petersen *et al.*, Temperature and salinity of the Late Cretaceous Western Interior Seaway. *Geology* **44**, 903–906 (2016).
67. T. J. Leutert *et al.*, Sensitivity of clumped isotope temperatures in fossil benthic and planktic foraminifera to diagenetic alteration. *Geochim. Cosmochim. Acta* **257**, 354–372 (2019).
68. S. V. Petersen, D. P. Schrag, Antarctic ice growth before and after the Eocene-Oligocene transition: New estimates from clumped isotope paleothermometry. *Paleoceanography* **30**, 1305–1317 (2015).
69. R. Caballero, M. Huber, State-dependent climate sensitivity in past warm climates and its implications for future climate projections. *Proc. Natl. Acad. Sci. U.S.A.* **110**, 14162–14167 (2013).
70. G. Danabasoglu, NCAR CESM2 model output prepared for CMIP6 PMIP midHolocene. Version 20190923. Earth System Grid Federation. <https://doi.org/10.22033/ESGF/CMIP6.7674>. Accessed 11 October 2021.
71. G. Danabasoglu, NCAR CESM2 model output prepared for CMIP6 PMIP midPliocene-eoi400. Version 20200110. Earth System Grid Federation. [10.22033/ESGF/CMIP6.7675](https://doi.org/10.22033/ESGF/CMIP6.7675). Accessed 11 October 2021.
72. EC-Earth Consortium (EC-Earth), EC-Earth-Consortium EC-Earth3-LR model output prepared for CMIP6 PMIP midHolocene. Version 20200919. Earth System Grid Federation. <https://doi.org/10.22033/ESGF/CMIP6.4801>. Accessed 11 October 2021.
73. EC-Earth Consortium (EC-Earth), EC-Earth-Consortium EC-Earth3-LR model output prepared for CMIP6 PMIP midPliocene-eoi400. Version 20210401. Earth System Grid Federation. <https://doi.org/10.22033/ESGF/CMIP6.4804>. Accessed 11 October 2021.
74. NASA Goddard Institute for Space Studies (NASA/GISS), NASA-GISS GISS-E2.1G model output prepared for CMIP6 PMIP midHolocene. Version 20190916. Earth System Grid Federation. [10.22033/ESGF/CMIP6.7225](https://doi.org/10.22033/ESGF/CMIP6.7225). Accessed 11 October 2021.
75. NASA Goddard Institute for Space Studies (NASA/GISS), NASA-GISS GISS-E2.1G model output prepared for CMIP6 PMIP midPliocene-eoi400. Version 20190626. Earth System Grid Federation. <https://doi.org/10.22033/ESGF/CMIP6.7227>. Accessed 11 October 2021.
76. C. Williams, D. Lunt, J. Singarayer, M. V. Guarino, NERC HadGEM3-GC31-LL model output prepared for CMIP6 PMIP midHolocene. Version 20210111. Earth System Grid Federation. <https://doi.org/10.22033/ESGF/CMIP6.12129>. Accessed 11 October 2021.
77. C. Williams, D. Lunt, J. Singarayer, M. V. Guarino, NERC HadGEM3-GC31-LL model output prepared for CMIP6 PMIP midPliocene-eoi400. Version 20210222. Earth System Grid Federation. <https://doi.org/10.22033/ESGF/CMIP6.12130>. Accessed 11 October 2021.
78. C. Guo *et al.*, NCC NorESM1-F model output prepared for CMIP6 PMIP midHolocene. Version 20190920. Earth System Grid Federation. [10.22033/ESGF/CMIP6.11591](https://doi.org/10.22033/ESGF/CMIP6.11591). Accessed 11 October 2021.
79. C. Guo *et al.*, NCC NorESM1-F model output prepared for CMIP6 PMIP midPliocene-eoi400. Version 20190920. Earth System Grid Federation. [10.22033/ESGF/CMIP6.11592](https://doi.org/10.22033/ESGF/CMIP6.11592). Accessed 11 October 2021.
80. J.-B. Ladant *et al.*, Paleogeographic controls on the evolution of Late Cretaceous ocean circulation. *Clim. Past* **16**, 973–1006 (2020).